



Targeting cellular senescence prevents age-related bone loss in mice

Joshua N Farr^{1,2}, Ming Xu^{1,2}, Megan M Weivoda^{1,2}, David G Monroe¹, Daniel G Fraser¹, Jennifer L Onken¹, Brittany A Negley¹, Jad G Sfeir¹ , Mikolaj B Ogrodnik¹, Christine M Hachfeld¹, Nathan K LeBrasseur¹, Matthew T Drake¹, Robert J Pignolo¹, Tamar Pirtskhalava¹, Tamara Tchkonja¹, Merry Jo Oursler¹, James L Kirkland¹ & Sundeep Khosla¹ 

Aging is associated with increased cellular senescence, which is hypothesized to drive the eventual development of multiple comorbidities¹. Here we investigate a role for senescent cells in age-related bone loss through multiple approaches. In particular, we used either genetic (i.e., the *INK-ATTAC* ‘suicide’ transgene encoding an inducible caspase 8 expressed specifically in senescent cells^{2–4}) or pharmacological (i.e., ‘senolytic’ compounds^{5,6}) means to eliminate senescent cells. We also inhibited the production of the proinflammatory secretome of senescent cells using a JAK inhibitor (JAKi)^{3,7}. In aged (20- to 22-month-old) mice with established bone loss, activation of the *INK-ATTAC* caspase 8 in senescent cells or treatment with senolytics or the JAKi for 2–4 months resulted in higher bone mass and strength and better bone microarchitecture than in vehicle-treated mice. The beneficial effects of targeting senescent cells were due to lower bone resorption with either maintained (trabecular) or higher (cortical) bone formation as compared to vehicle-treated mice. *In vitro* studies demonstrated that senescent-cell conditioned medium impaired osteoblast mineralization and enhanced osteoclast-progenitor survival, leading to increased osteoclastogenesis. Collectively, these data establish a causal role for senescent cells in bone loss with aging, and demonstrate that targeting these cells has both anti-resorptive and anabolic effects on bone. Given that eliminating senescent cells and/or inhibiting their proinflammatory secretome also improves cardiovascular function⁴, enhances insulin sensitivity³, and reduces frailty⁷, targeting this fundamental mechanism to prevent age-related bone loss suggests a novel treatment strategy not only for osteoporosis, but also for multiple age-related comorbidities.

The accumulation of DNA damage and/or other cellular stressors (for example, oncogenic insults, reactive metabolites, and proteotoxic stress)^{1,8–10} causes proliferating cells^{11,12}, as well as terminally differentiated, nondividing cells^{13–16}, to undergo senescence, a process

characterized by profound chromatin and secretome changes. Cellular senescence is also associated with increased expression of the senescence biomarker *p16^{Ink4a}* (also known as *Cdkn2a*) and resistance to apoptosis^{1,17}. In addition, senescent cells can develop the senescence-associated secretory phenotype (SASP), consisting of proinflammatory cytokines, chemokines, and extracellular matrix-degrading proteins, which have deleterious paracrine and systemic effects^{3,18–20}. Indeed, even a relatively low abundance of senescent cells (for example, ~10–15% in aged primates²¹) is sufficient to cause tissue dysfunction. We recently demonstrated that with aging, multiple cell types in the bone microenvironment become senescent, although senescent myeloid cells and senescent osteocytes predominantly develop the SASP¹⁶. Consistent with this, further characterization revealed that *p16^{Ink4a}* expression in mouse osteocytes increases markedly after ~18 months of age in both sexes (Supplementary Fig. 1a,b), coinciding with the timing of accelerated age-related bone loss in both female and male mice (Supplementary Fig. 1c–j)^{22,23}.

Eliminating a relatively small proportion (~30%) of senescent cells using a ‘suicide’ transgene, *INK-ATTAC*, that permits inducible elimination of *p16^{Ink4a}*-expressing senescent cells upon the administration of a drug (AP20187; Supplementary Fig. 2) extends health span and prevents the development of multiple age-related morbidities in both progeroid and normal, chronologically aged mice^{2–4}. However, the skeletal phenotype of these animals has not been characterized, and the potential role of senescent cells in age-related bone loss has not been investigated. To test the hypothesis that senescent cells mediate age-related bone loss, female *INK-ATTAC* transgenic mice^{2–4} were randomized to either vehicle or AP20187 treatment twice weekly for 4 months, starting at 20 months of age (Fig. 1a). As anticipated, AP20187 treatment resulted in markedly lower *p16^{Ink4a}* mRNA expression (by ~59%) in bone relative to that in vehicle-treated mice (Fig. 1b), as well as lower enhanced green fluorescent protein (EGFP) mRNA (by ~48%) encoded by the *INK-ATTAC* transgene^{2–4} (Fig. 1c), consistent with the clearance of senescent cells. This was confirmed by a finding of fewer senescent osteocytes in AP20187-treated relative to vehicle-treated mice (by ~46%), as assessed by an established

¹Robert and Arlene Kogod Center on Aging and Division of Endocrinology, Mayo Clinic College of Medicine, Rochester, Minnesota, USA. ²These authors contributed equally to this work. Correspondence should be addressed to S.K. (khosla.sundeep@mayo.edu) or J.L.K. (kirkland.james@mayo.edu).

Received 4 April; accepted 13 July; published online 21 August 2017; corrected after print 11 October 2017; doi:10.1038/nm.4385

senescence biomarker (senescence-associated distention of satellites (SADS)^{9,16} (Fig. 1d–f); see **Supplementary Fig. 3** and legend for a further, detailed *in vitro* validation of the SADS assay using primary osteocyte cultures)^{9,16}. Note that we used three measures of senescent-cell burden in bone (*p16^{Ink4a}* mRNA, *EGFP* mRNA encoded by the *INK-ATTAC* transgene, and SADS-positive osteocytes), all with concordantly lower values in AP20187-treated than in vehicle-treated mice. The systemic clearance of senescent cells by AP20187 treatment was further demonstrated by lower *p16^{Ink4a}* (Fig. 1g) and *EGFP* (Fig. 1h) mRNA levels in adipose tissue.

Relative to vehicle treatment, AP20187-treated mice had better spine trabecular bone microarchitecture (for example, a 52% higher bone volume/total volume (BV/TV)); (Fig. 1i–n), and demonstrated similar improvements in trabecular bone at the femur (**Supplementary Fig. 4a–f**). AP20187 treatment also resulted in significantly higher cortical thickness and bone strength (by microfinite element analysis (μFEA)) at the femur (Fig. 1o–q). In addition and in keeping with the μFEA results, we found substantially better caudal vertebrae bone biomechanical properties (as assessed by biomechanical testing²⁴) in AP20187-treated as compared to vehicle-treated mice (**Supplementary Fig. 5a–e**), whereas bone material properties (as assessed by nano-indentation testing^{25,26}) were not different between AP20187- and vehicle-treated mice (**Supplementary Fig. 5f,g**).

In contrast to the treatment of aged mice, treatment of young adult (12-month-old) *INK-ATTAC* mice with AP20187 did not alter bone parameters (**Supplementary Fig. 6a–o**), indicating that this strategy is specific to the prevention of age-related bone loss. Trabecular bone histomorphometry in the old *INK-ATTAC* mice demonstrated significantly lower bone resorption (osteoclast numbers per bone perimeter, $P < 0.001$; **Supplementary Fig. 7a**) in AP20187-treated relative to vehicle-treated mice, without a coupled reduction in bone-formation indices (osteoblast numbers, mineral apposition rate, and bone formation rate (**Supplementary Fig. 7b–d**)). We excluded possible direct effects of AP20187 on osteoclasts by demonstrating that whereas the administration of treatment for 4 months in old *INK-ATTAC* mice resulted in significantly lower concentrations of the circulating bone resorption marker, C-terminal telopeptide of type I collagen (CTX, $P < 0.01$), treatment of young *INK-ATTAC* mice for either 1.5 months or 4 months had no effect on CTX levels (**Supplementary Fig. 8a**). In addition, *in vitro* treatment of mature osteoclasts generated from the *INK-ATTAC* mouse bone marrow using AP20187 did not induce osteoclast apoptosis (**Supplementary Fig. 8b–d**). Despite these findings, however, it is still possible that with aging, a subset of osteoclasts becomes senescent and may be directly cleared by AP20187, thereby contributing to the observed inhibition of bone resorption.

Osteoblast numbers were markedly lower in aged as compared to young mice and were unchanged by AP20187 treatment (**Supplementary Fig. 8e**). By contrast, AP20187 treatment resulted in significantly lower osteoclast numbers ($P < 0.001$; **Supplementary Fig. 8f**), resulting in an improvement in the osteoblast/osteoclast ratio in aged AP20187-treated mice (**Supplementary Fig. 8g**). The lower bone resorption in AP20187-treated as compared to vehicle-treated mice was also evident on the endocortical surface of the femur (Fig. 1r); additionally, on this surface, osteoblast numbers, mineral apposition rate, and bone-formation rate were all higher in the AP20187-treated mice than in the vehicle-treated ones (Fig. 1s–u), thus suggesting that the accumulation of senescent cells led to an impairment in bone formation that was improved by their clearance. To further test this, osteoblastic MC3T3 cells (a cell line derived from mouse calvaria)

were exposed to conditioned medium (CM) collected from control or senescent cells. Senescent cell CM treatment markedly impaired the mineralization of MC3T3 cells as compared to that of control CM (Fig. 1v,w). Therefore, the reduction in senescent cell burden in aged (but not young) mice using a genetic approach resulted in improved trabecular- and cortical-bone parameters associated with lower bone resorption, and either maintained (trabecular) or increased (cortical) bone formation. To further define potential mechanisms, we assessed mRNA expression of key regulators of bone formation (*Sost*) and bone resorption (*Tnfrs11b* (*Opg*), and *Tnfsf11* (*Rankl*)) in osteocyte-enriched bones^{16,27} from these mice and found significantly lower *Sost* mRNA expression in AP20187-treated relative to vehicle-treated mice ($P < 0.001$; **Supplementary Fig. 9a–d**). Clearance of senescent cells also resulted in significantly lower numbers, perimeter, and volume/tissue volume of bone marrow adipocytes (all $P < 0.01$; **Supplementary Fig. 9e–g**).

As an alternative to the genetic approach and one potentially applicable to humans, we have exploited the dependence of senescent cells on specific prosurvival pathways and identified a combination of senolytics—dasatinib (D; an FDA-approved tyrosine kinase inhibitor²⁸) and quercetin (Q; a flavanol present in many fruits and vegetables²⁹)—that specifically kills senescent cells without affecting proliferating or quiescent, differentiated cells^{5,6}. To test this approach, 20-month-old male C57BL/6 mice were randomized to either vehicle or D + Q treatment once monthly for 4 months (Fig. 2a). D + Q treatment led to significantly lower *p16^{Ink4a}* mRNA in bone (Fig. 2b), as well as a lower percentage of senescent osteocytes, as assessed by a SADS assay (Fig. 2c), in D + Q-treated mice relative to vehicle-treated mice. The systemic clearance of senescent cells with D + Q was verified by demonstrating lower *p16^{Ink4a}* mRNA (Fig. 2d) and SA-β-gal-positive cells (Fig. 2e–g) in adipose tissue of 24-month-old D + Q-treated mice. As in the *INK-ATTAC* model, D + Q administration for 4 months resulted in substantially better spine trabecular bone microarchitecture than in vehicle-treated controls (Fig. 2h–m), with similar improvements in trabecular bone at the femur (**Supplementary Fig. 10a–f**). Similarly to the *INK-ATTAC* model, trabecular bone histomorphometry demonstrated lower osteoclast numbers per bone perimeter in D + Q-treated than in vehicle-treated mice (**Supplementary Fig. 10g**), and there were no differences in osteoblast numbers, mineral apposition rate, or bone-formation rate (**Supplementary Fig. 10h–j**). Also similarly to the *INK-ATTAC* model, D + Q treatment resulted in higher femur cortical thickness and μFEA-derived bone strength (Fig. 2n–p). This was associated with lower osteoclast numbers on the endocortical surface (Fig. 2q), along with higher endocortical osteoblast numbers (Fig. 2r), mineral-apposition rate (Fig. 2s), and bone-formation rate (Fig. 2t). Thus, both the genetic (*INK-ATTAC*) and pharmacological (D + Q) approaches for clearing senescent cells led to virtually identical improvements in trabecular and cortical bone microarchitecture, demonstrating similar underlying cellular mechanisms in trabecular and cortical bone compartments.

Because senescent-cell clearance was associated with lower osteoclast numbers and bone resorption *in vivo*, we next tested the direct effects of senescent cells on osteoclastogenesis. Pre-treatment of whole-mouse bone marrow with senescent-cell CM resulted in greater osteoclast differentiation potential of nonadherent marrow cells than that achieved by control CM pre-treatment, as evidenced by the markedly higher number of tartrate-resistant acid phosphatase (TRAP)-positive, multinucleated osteoclasts (Fig. 3a,b). The senescent cell CM-treated osteoclast differentiation cultures also exhibited

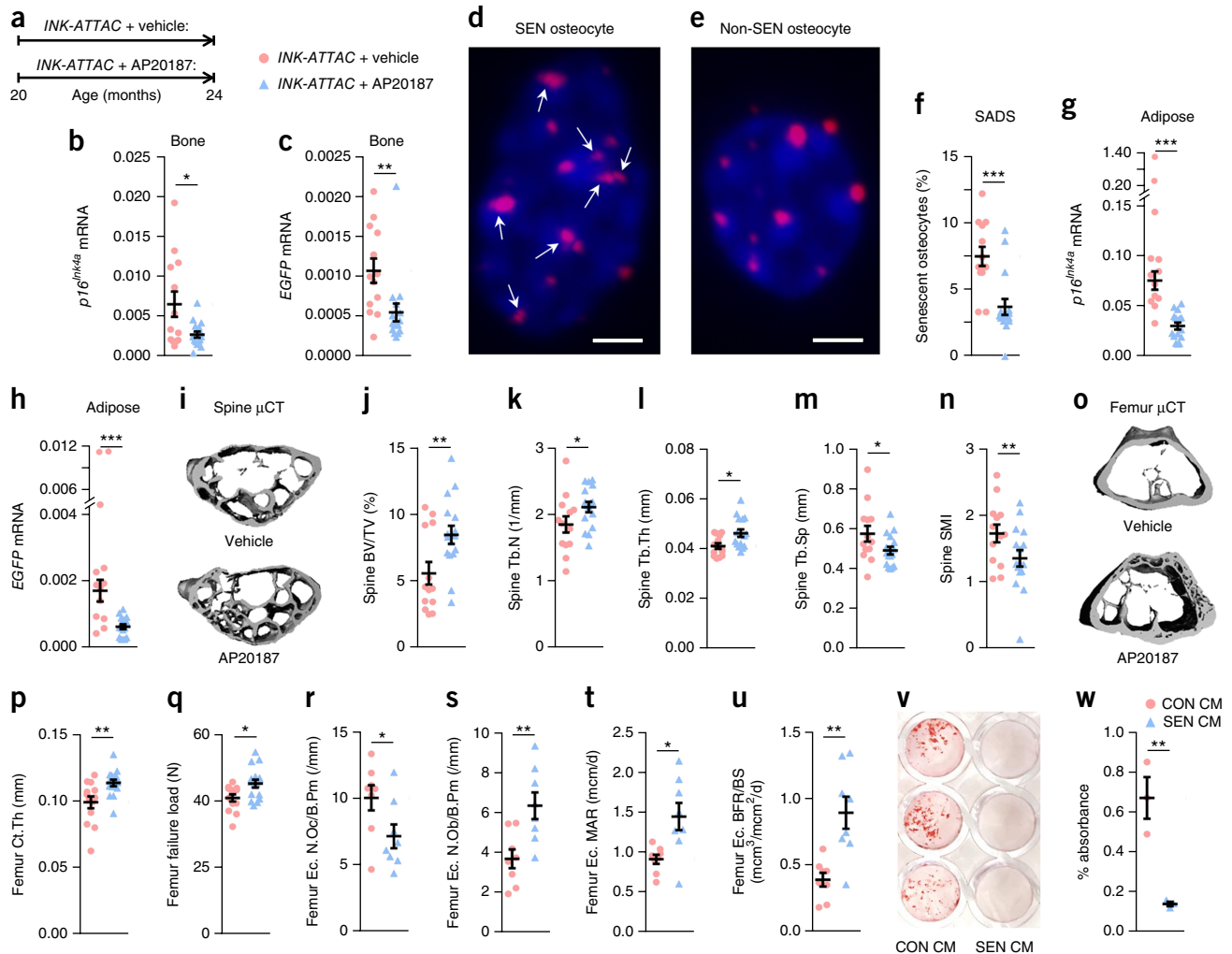


Figure 1 Clearance of $p16^{Ink4a+}$ senescent cells prevents age-related bone loss. (a) Experimental design for testing the effect of senescent cell clearance using a transgenic approach on age-related bone loss: 20-month-old female *INK-ATTAC* mice were randomized to either vehicle ($n = 13$) or AP20187 ($n = 16$) treatments (intraperitoneally (i.p.) twice weekly) for 4 months. (b,c) RT-qPCR analysis of $p16^{Ink4a}$ (b) and *EGFP* (encoded by the *INK-ATTAC* transgene) (c) mRNA expression levels in osteocyte-enriched cells derived from the bones of mice. (d,e) Representative images ($n > 30$ images per animal, 13 vehicle-treated and 16 AP20187-treated) of a senescent (SEN) osteocyte (magnification, 100 \times) (d) versus a nonsenescent (non-SEN) osteocyte (magnification, 100 \times) (e) according to the senescence-associated distention of satellites (SADS, see arrows in d) assay in cortical bone diaphysis (scale bars, 2 μ m). (f) Quantification of the percentage of senescent osteocytes in mice treated with either vehicle or AP20187 according to the SADS assay. (g,h) RT-qPCR analysis of $p16^{Ink4a}$ (g) and *EGFP* (h) mRNA expression levels in perigonadal adipose tissue. (i) Representative microcomputed tomography (μ CT) images ($n = 13$ vehicle-treated and 16 AP20187-treated mice) of bone microarchitecture at the lumbar spine of vehicle-treated versus AP20187-treated mice. (j–n) Quantification of μ CT-derived bone volume fraction (BV/TV; %) (j), trabecular number (Tb.N; 1/mm) (k), trabecular thickness (Tb.Th; mm) (l), trabecular separation (Tb.Sp; mm) (m), and structure model index (SMI, a measure of plate/rod morphology, with lower numbers being better) (n) at the lumbar spine. (o) Representative μ CT images ($n = 13$ vehicle-treated and 16 AP20187-treated mice) of bone microarchitecture at the femur. (p,q) Quantification of μ CT-derived cortical thickness (Ct.Th; mm) (p) and micro-finite-element analysis (μ FEA)-derived failure load (N, Newton (i.e., a measure of bone strength)) (q). (r–u) Histomorphometric quantification at the femoral endocortical surface of osteoclast numbers per bone perimeter (N.Oc/B.Pm; /mm) (r), osteoblast numbers per bone perimeter (N.Ob/B.Pm; /mm) (s), endocortical mineral apposition rate (MAR; mcm/d) (t), and endocortical bone formation rate per bone surface (BFR/BS; mcm³/mcm²/d) (u); $n = 8$ /group. (v,w) Mineralization of osteoblastic MC3T3 cells exposed to control (CON) or senescent (SEN) conditioned medium (CM) ($n = 3$ /group) (v), with quantification of eluted alizarin red dye (w). Data represent mean \pm s.e.m. (error bars). * $P < 0.05$; ** $P < 0.01$; *** $P < 0.001$ (independent samples t -test or Wilcoxon rank-sum test, as appropriate).

significantly higher mRNA expression of the osteoclast markers *Ctsk*, *Oc-stamp*, *Oscar*, *Tnfrsf11a* (*RANK*), and *Acp5* (*Trap*) (Fig. 3c).

To determine the mechanism underlying the increase in osteoclastogenic potential, nonadherent bone marrow cells were assessed following CM pre-treatment. Flow cytometry demonstrated that the percentage of early osteoclast progenitor cells (defined as CD115 (monocyte marker)⁺/receptor activator of nuclear factor (NF)- κ B (RANK⁺)) was higher by more than two-fold in cells

exposed to senescent-cell CM relative to those exposed to control CM (Fig. 3d,e). Given that RANK expression increases with osteoclast differentiation³⁰, these data indicate that senescent-cell CM increased the number of early monocyte osteoclast progenitors that had not yet acquired RANK expression. This increase was due to enhanced survival, given that apoptosis was significantly lower in whole marrow (Fig. 3f), as well as in monocyte-enriched cultures (Fig. 3g), exposed to senescent-cell versus control CM. Senescent-cell

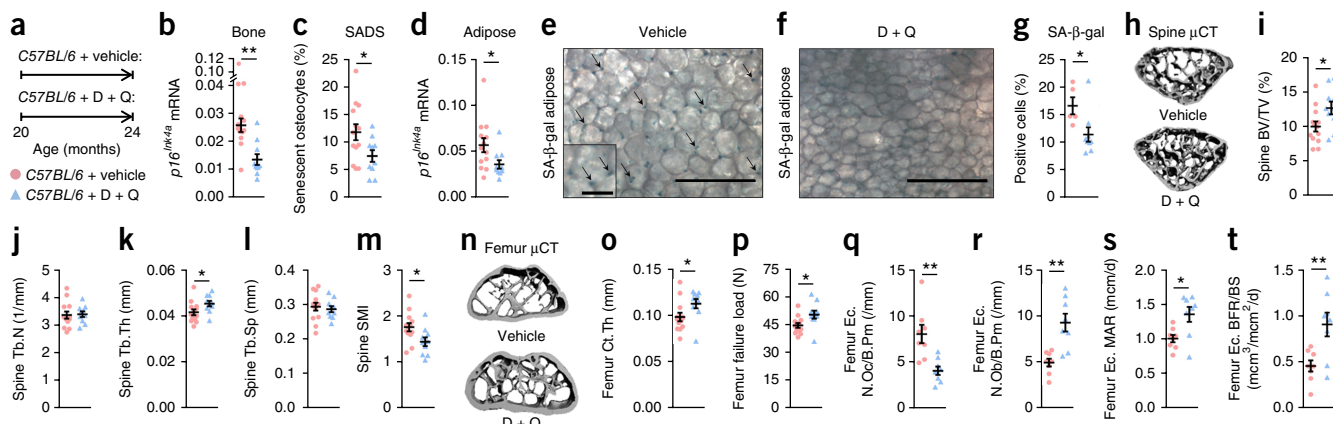


Figure 2 Senescent-cell clearance by treatment with senolytics (D + Q) prevents age-related bone loss. (a) Experimental design for testing the effect of senescent cell clearance through periodic treatment with D + Q on age-related bone loss: 20-month-old male C57BL/6 mice were randomized to either vehicle (*n* = 13) or D + Q (*n* = 10) treatments (once monthly by oral gavage) for 4 months. (b) RT-qPCR analysis of *p16^{Ink4a}* mRNA expression levels in osteocyte-enriched cells derived from bones. (c) Quantification of the percentage of senescent osteocytes in cortical bone diaphysis using the SADS assay. (d–g) Analysis of perigonadal adipose tissue *p16^{Ink4a}* mRNA expression levels (d), and staining for senescence-associated β-galactosidase (SA-β-gal) positive cells (e, vehicle; f, D + Q) (see arrows (in e); magnification, 10×; scale bars, 400 μm; 100 μm in inset (in e)), with quantification of the percentage of SA-β-gal-positive cells (g). (h) Representative μCT images (*n* = 13 vehicle-treated and 10 D + Q-treated mice) of bone microarchitecture at the lumbar spine of vehicle-treated versus D + Q-treated male C57BL/6 mice. (i–m) Quantification of μCT-derived bone volume fraction (BV/TV; %) (i), trabecular number (Tb.N; 1/mm) (j), trabecular thickness (Tb.Th; mm) (k), trabecular separation (Tb.Sp; mm) (l), and structure model index (SMI) (m) at the lumbar spine. (n) Representative μCT images (*n* = 13 vehicle-treated and 10 D + Q-treated mice) of bone microarchitecture at the femur. (o,p) Quantification of μCT-derived cortical thickness (Ct.Th; mm) (o) and failure load (N) (p). (q–t) Histomorphometric quantification at the femoral endocortical surface of osteoclast numbers per bone perimeter (N.Oc/B.Pm; /mm) (q), osteoblast numbers per bone perimeter (N.Ob/B.Pm; /mm) (r), endocortical mineral apposition rate (MAR; mcm/d) (s), and endocortical bone formation rate per bone surface (BFR/BS; mcm³/mcm²/d) (t) (*n* = 8/group). Data represent mean ± s.e.m. (error bars). **P* < 0.05; ***P* < 0.01; ****P* < 0.001 (independent samples *t*-test or Wilcoxon rank-sum test, as appropriate).

CM pre-treatment did not alter the differentiation of monocyte-enriched cultures plated at equal densities, indicating no direct effect of senescent-cell CM on monocyte differentiation into osteoclasts (Supplementary Fig. 11a).

We have previously shown that the JAKi ruxolitinib attenuates the production of multiple SASP components by senescent cells^{3,7}. Consistent with this, CM from JAKi-treated senescent cells exhibited a markedly reduced ability to promote osteoclast differentiation as compared to CM from senescent cells (Fig. 3h,i). This effect was due to JAKi effects on senescent-cell SASP secretion, because adding the JAKi directly to senescent-cell CM did not affect osteoclastogenesis (Supplementary Fig. 11b,c). In our earlier study⁷, we identified interleukin (IL)-6, IL-8 (human homolog to mouse CXCL1), and plasminogen activator inhibitor-1 (PAI-1) as the most critical components of the SASP that were markedly downregulated by JAK inhibition; because these cytokines also modulate bone resorption^{31–33}, we next used neutralizing antibodies to each of them, which revealed that, as compared to an IgG control, neutralization of each of these SASP components attenuated the pro-osteoclastogenic effects of senescent-cell CM (Fig. 3j).

To test the effects of SASP inhibition *in vivo* on age-related bone loss, 22-month-old male C57BL/6 mice were treated with ruxolitinib for 2 months (Fig. 4a). Relative to vehicle-treated mice, JAKi-treated mice had better spine trabecular-bone microarchitecture (Fig. 4b–g), with similar differences in the femur (Fig. 4h–m). JAKi treatment also resulted in significantly higher bone strength of the femur (Fig. 4n). By contrast, 2 months of treatment of young adult male C57BL/6 mice (7 months old) with the JAKi did not alter bone parameters (Supplementary Fig. 12), indicating that this strategy is specific to the prevention of age-related bone loss. Similarly to the trabecular-bone histomorphometry findings following the

reduction of senescent cells using the *INK-ATTAC* suicide transgene or following D + Q treatment, trabecular-bone histomorphometry in the JAKi-treated aged mice revealed significantly lower osteoclast numbers per bone perimeter as compared to vehicle-treated mice (Fig. 4o), with no significant differences in osteoblast numbers (Fig. 4p). *Ex vivo* analysis of bone marrow revealed significantly lower osteoclast progenitor colony-forming units (CFU)–granulocyte monocyte (CFU-GM) (*P* < 0.01) and CFU monocytes (CFU-M) (*P* < 0.05; Supplementary Fig. 13a,b). In addition, bone marrow isolated from aged JAKi-treated mice had significantly impaired osteoclastogenic potential as compared to vehicle treatment (*P* < 0.001; Supplementary Fig. 13c,d); consistent with a lack of effect of the JAKi on skeletal parameters in young mice, the osteoclastogenic potentials of bone marrow from young vehicle-treated and JAKi-treated mice were virtually identical (Supplementary Fig. 13e). Finally, to further validate our *in vitro* findings, we also measured circulating levels of IL-6, CXCL1 (IL-8), and PAI-1 in the vehicle-treated and JAKi-treated mice, and, as shown in Supplementary Figure 14a, all three cytokines were lower in the JAKi-treated than in the vehicle-treated mice. By contrast, these cytokines were not lower in plasma from *INK-ATTAC* (Supplementary Fig. 14b) or D + Q-treated (Supplementary Fig. 14c) mice, suggesting that the JAKi has more systemic effects on the SASP, whereas changes in SASP factors following the specific elimination of senescent cells may be more localized to their microenvironment.

Age-related cellular senescence has been causally linked to declining cardiovascular and metabolic function^{3,4}, as well as to frailty⁷. Here we examine another major aging comorbidity, osteoporosis, and establish the causal role of senescence in age-related bone loss. We use three different approaches to attenuate both the systemic and paracrine detrimental effects of senescent cells in 20- to 22-month-old

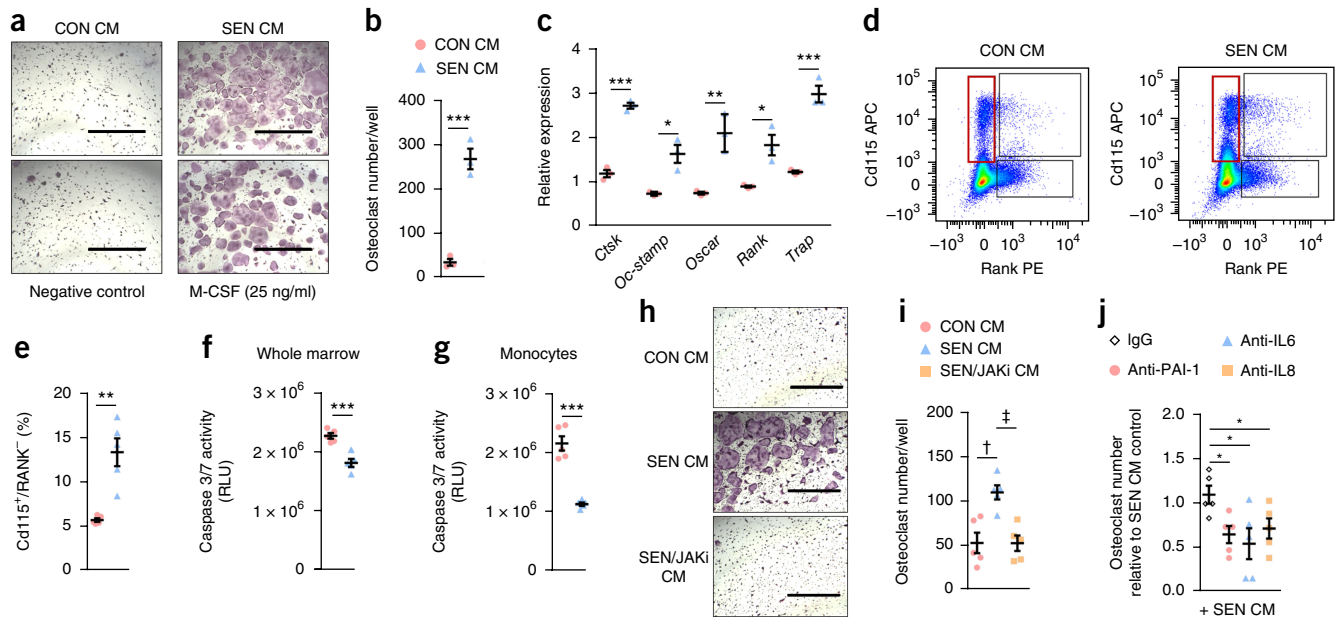


Figure 3 The SASP increases osteoclastogenesis *in vitro* by promoting the survival of monocyte osteoclast progenitors. (a) Representative images (from three individual sets of cell cultures) of tartrate-resistant acid phosphatase (TRAP)-stained osteoclast cultures (magnification, 4 \times ; scale bars, 1,000 μ m) pre-treated with vehicle (negative control), M-CSF (25 ng/ml), control (CON) conditioned medium (CM), or senescent (SEN) CM ($n = 3$ /group). (b) Osteoclast numbers per well following 4 d of osteoclast differentiation of bone marrow cells pre-treated with CON CM or SEN CM following 2 d of osteoclast differentiation; gene expression was denoted as fold-change relative to vehicle (negative control) pre-treated osteoclast cultures ($n = 3$ /group). (c) RT-qPCR analysis of osteoclast genes in bone marrow cells pre-treated with CON CM or SEN CM following 2 d of osteoclast differentiation; gene expression was denoted as fold-change relative to vehicle (negative control) pre-treated osteoclast cultures ($n = 3$ /group). (d,e) Flow cytometric analysis of CD115 $^{+}$ (monocyte marker) and Rank $^{+}$ (osteoclast progenitor marker) cells in nonadherent population after 24 h of treatment with CON CM or SEN CM. (d) Representative images (from five individual sets of cell cultures) of flow cytometric gating with the CD115 $^{+}$ /Rank $^{+}$ monocyte population outlined in red (5.4% in CON CM and 14.2% in SEN CM). (e) Average CD115 $^{+}$ /Rank $^{+}$ percentages in CON CM versus SEN CM ($n = 5$ /group; see **Supplementary Fig. 15** for flow cytometry gating strategy). (f,g) Apoptosis, as measured by cleavage of a luminogenic caspase-3/7 substrate (RLU), in whole marrow (f) and monocyte-enriched cultures (g) following 24 h of treatment with CON CM or SEN CM ($n = 5$ /group). (h,i) Representative images (from five individual sets of cell cultures) of TRAP-stained osteoclast cultures (magnification, 4 \times ; scale bars, 1,000 μ m) (h) and osteoclast numbers per well (i) after 3 d of osteoclast differentiation of bone marrow cells pre-treated with CON CM, SEN CM, or CM from senescent cells treated with 0.6- μ M JAKi (SEN/JAKi) ($n = 5$ /group). (j) Osteoclast numbers per well after 3 d of osteoclast differentiation of bone marrow cells pre-treated with SEN CM in the presence of control IgG (20 μ g/ml), anti-PAI-1 (5 μ g/ml), anti-IL-6 (5 μ g/ml), or anti-IL-8 (20 μ g/ml) ($n = 5$ /group); osteoclast numbers are expressed relative to SEN CM control. Data represent mean \pm s.e.m. (error bars). * $P < 0.05$; ** $P < 0.01$; *** $P < 0.001$ (independent samples *t*-test or Wilcoxon rank-sum test, as appropriate); $^{\dagger}P < 0.01$ (one-way analysis of variance (ANOVA) versus CON CM followed by Bonferroni *post hoc* test); $^{\ddagger}P < 0.01$ one-way (ANOVA versus SEN CM followed by the Bonferroni *post hoc* test).

mice, which have substantial bone loss that mimics osteoporosis in elderly humans. Concomitant with reducing the burden of senescent cells (genetically or pharmacologically) or with inhibiting the production of the SASP by senescent cells (pharmacologically), we demonstrate a markedly better skeletal phenotype, relative to vehicle treatment, with all three approaches. Using bone histomorphometry, we further demonstrate that targeting senescent cells results in lower bone resorption. Importantly, despite lower bone resorption, bone formation is either maintained (trabecular bone) or is higher (cortical bone) following reduction of the senescent-cell burden. The inhibition of bone resorption without a concomitant reduction, or an actual stimulation, in bone formation resulting from targeting senescent cells is in contrast to all currently available anti-resorptive drugs for osteoporosis (bisphosphonates, denosumab, estrogen, or raloxifene), in which a reduction in bone resorption is uniformly associated with a reduction in bone formation³⁴. The only other drugs to inhibit bone resorption with comparatively lesser effects on bone formation than bisphosphonates or denosumab were the cathepsin-K inhibitors³⁴. Unfortunately, the development of this pharmacologic class has recently been halted, owing to an unforeseen increase in stroke risk in a large, phase 3 odanacatib trial³⁵. Importantly, new drugs such as senolytics, which inhibit bone

resorption without a concomitant reduction in bone formation, would be expected to be efficacious in treating age-related osteoporosis, because the 'pure' anti-resorptive bisphosphonate zoledronic acid increased bone mineral density and reduced subsequent vertebral and nonvertebral fractures in a group of women and men with a mean age of ~75 years³⁶.

It should be noted that, on the basis of the availability of very old mice from the National Institute on Aging mouse colony, female mice were used in the *INK-ATTAC* study, whereas male mice were used in the *D + Q* and *JAKi* studies. This accounts for the differences in BV/TV in the vehicle-treated mice in the three studies. Given that qualitatively similar effects were seen using all three approaches in different sexes, it could be argued that this strengthens our conclusions.

In our previous work¹⁶, we found that multiple cell types in the bone microenvironment, including hematopoietic cells, had increased *p16^{Ink4a}* expression with aging. Moreover, not only senescent osteocytes, but also senescent myeloid cells, developed the SASP. Because none of our three approaches was cell-specific, whether the elimination of senescent hematopoietic (for example, myeloid cells) or senescent mesenchymal cells (for example, osteocytes) was specifically responsible for the beneficial effects of reducing senescent cell burden or the SASP on skeletal parameters in mice with

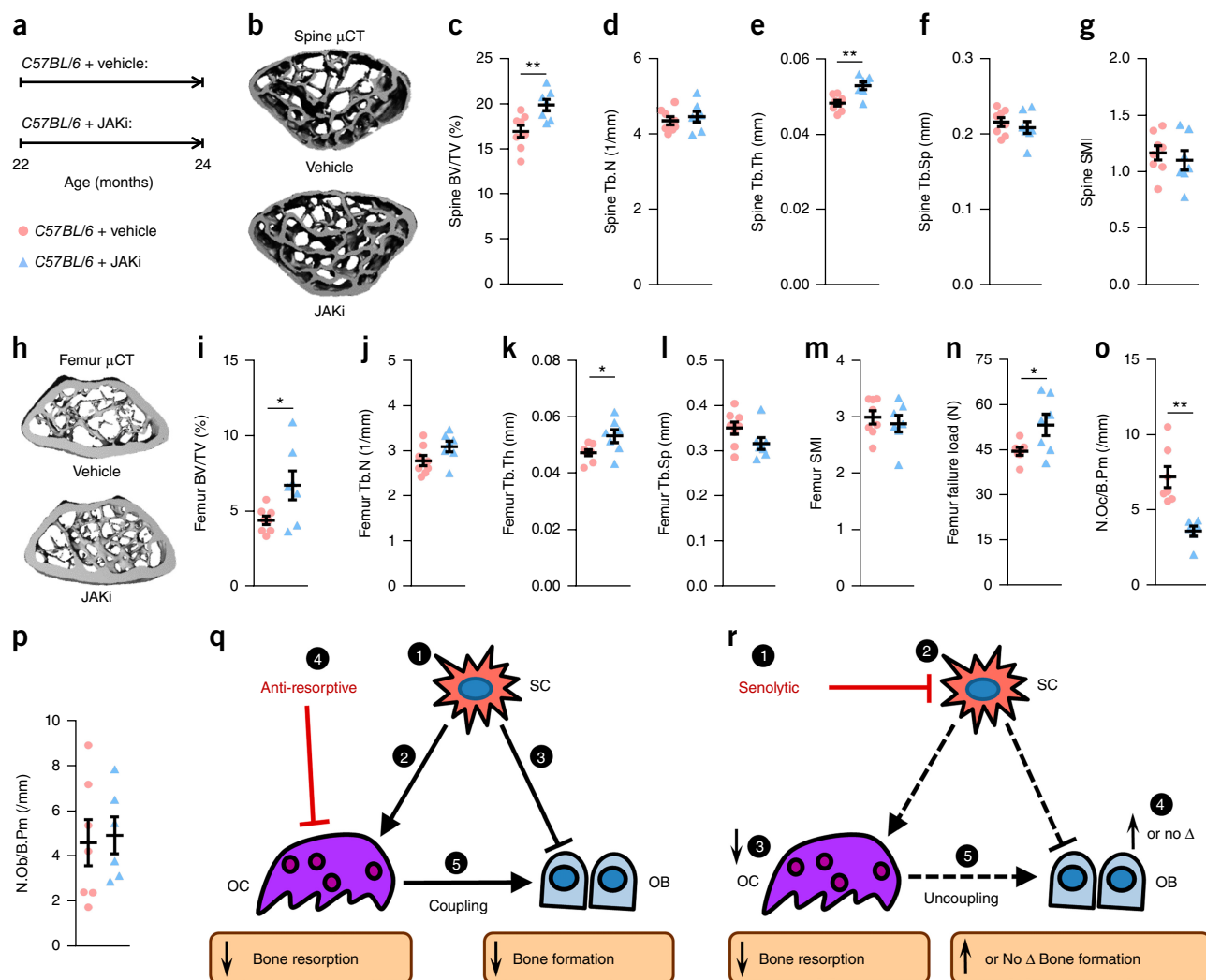


Figure 4 Suppression of the SASP by treatment with the JAK1/2 inhibitor ruxolitinib prevents age-related bone loss. (**a**) Experimental design for testing the effect of SASP inhibition induced by ruxolitinib on age-related bone loss: 22-month-old male C57BL/6 mice were randomized to either vehicle ($n = 8$) or JAKi ($n = 7$) treatments daily for 2 months. (**b**) Representative μ CT images of bone microarchitecture at the lumbar spine ($n = 8$ vehicle-treated and $n = 7$ JAKi-treated mice). (**c–g**) Quantification of μ CT-derived bone volume fraction (BV/TV; %) (**c**), trabecular number (Tb.N; 1/mm) (**d**), trabecular thickness (Tb.Th; mm) (**e**), trabecular separation (Tb.Sp; mm) (**f**), and SMI (**g**). (**h**) Representative μ CT images ($n = 8$ vehicle-treated and $n = 7$ JAKi-treated mice) of bone microarchitecture at the femoral metaphysis. (**i–n**) Quantification of femoral metaphysis μ CT-derived BV/TV (%) (**i**), Tb.N (1/mm) (**j**), Tb.Th (mm) (**k**), Tb.Sp (mm) (**l**), SMI (**m**), and failure load (N) (**n**). Femoral metaphysis trabecular quantification of osteoclast numbers per bone perimeter (N.Oc/B.Pm; 1/mm) (**o**) and osteoblast number per bone perimeter (N.Ob/B.Pm; 1/mm) (**p**). Data represent mean \pm s.e.m. (error bars). $*P < 0.05$; $**P < 0.01$; $***P < 0.001$ (independent samples t -test). (**q, r**) Comparing the effects of anti-resorptive versus senolytic therapies on bone metabolism. (**q**) (1) Senescent cells (SCs) accumulate in the bone microenvironment with aging, where they (2) increase bone resorption by osteoclasts (OCs) and (3) decrease bone formation by osteoblasts (OBs). (4) Anti-resorptive therapy inhibits or eliminates OCs and decreases bone resorption; owing to (5) coupling, there is a concomitant reduction in bone formation. (**r**) (1) Senolytic therapy reduces the burden of (2) SCs, which in turn (3) suppresses bone resorption with (4) either an increase (cortical bone) or maintenance (trabecular bone) in bone formation, leading to (5) uncoupling between OCs and OBs.

aging will require further study. In addition, it is possible that the skeletal effects of targeting senescent cells are due to changes occurring outside of bone, through systemic factors such as cytokines, growth factors, or hormones.

Although clearing senescent cells using a genetic approach is not feasible in humans, the two pharmacological approaches described here are clearly translatable. Although JAK inhibition does have effects on multiple tissues⁷, and effects of the JAKi besides SASP inhibition could be contributing to its skeletal effects, suppressing the SASP to enhance bone mass is indeed novel, and other potentially emerging compounds that have similar actions in bone without deleterious

effects in other tissues could be translated to the clinic. Moreover, targeting senescent cells using senolytic drugs is another viable, translatable approach. This is because these drugs would need to be given only intermittently, thereby killing senescent cells without inducing other, off-target effects. Note that in our study, D + Q were administered once monthly, thereby minimizing possible effects related to pathways other than their senolytic effects. In addition, on the basis of prosurvival pathways previously shown to confer apoptosis resistance to senescent cells^{5,6}, additional senolytic agents such as the Bcl-2 family inhibitor navitoclax (ABT263)³⁷, have been identified. Regardless of which specific senolytic compounds are eventually used for

osteoporosis and other aging morbidities, our study provides a critical proof of concept for the feasibility of this approach for treatment of age-related bone loss.

In conclusion, osteoporosis is an enormous public-health problem that will only increase in scope with the aging of the population³⁸. In addition to the morbidity associated with fractures, up to 25% of elderly individuals who have experienced hip fractures die within a year of this devastating event³⁹. Thus, there is a crucial need to identify novel therapeutic paradigms for age-related bone loss. The approaches identified here for either eliminating senescent cells or suppressing their SASP represent, to our knowledge, the first therapeutic paradigm to treat age-related osteoporosis by targeting not just bone-specific pathways, as with all currently available (or soon to be available) drugs, but rather by targeting a fundamental aging mechanism present in all tissues. Indeed, whereas conventional anti-resorptive therapy predominantly targets osteoclasts to decrease bone resorption, with a concomitant decrease in bone formation owing to coupling (Fig. 4q), senolytics reduce senescent-cell burden, which in turn suppresses bone resorption with either an increase (cortical bone) or maintenance (trabecular bone) in bone formation (Fig. 4r). Furthermore, eliminating senescent cells or inhibiting the production of their SASP has been shown to improve cardiovascular function⁴, enhance insulin sensitivity³, and reduce frailty⁷ in old mice. The present work demonstrates that a similar approach may also be useful for treating osteoporosis, making it fundamentally different from all current therapies for osteoporosis, which benefit bone only. Therefore, therapeutically targeting senescent cells would not only be a novel strategy for treating osteoporosis by simultaneously reducing bone resorption and enhancing bone formation, but also for concurrently preventing multiple aging comorbidities by targeting a fundamental aging mechanism.

METHODS

Methods, including statements of data availability and any associated accession codes and references, are available in the [online version of the paper](#).

Note: Any Supplementary Information and Source Data files are available in the online version of the paper.

ACKNOWLEDGMENTS

This work was supported by NIH grants P01 AG004875 (S.K.), R01 AG048792 (S.K.), K01 AR070241 (J.N.F.), K01 AR070281 (M.M.W.), R01 AR068275 (D.G.M.), R37 AG013925 (J.L.K.), AG R21 049182 (J.L.K.), the Connor Group, the Noaber, and the Ted Nash Foundations (J.L.K.), the Glenn Foundation (J.L.K., N.K.L.), and both a High-Risk Pilot Award (J.N.F. and S.K.) and Career Development Awards (J.N.F. and M.M.W.) from the Mayo Clinic Robert and Arlene Kogod Center on Aging, as well as the Richard F. Emslander Career Development Award in Endocrinology (J.N.F.), the James A. Ruppe Career Development Award in Endocrinology (M.M.W.), and the Glenn/American Federation for Aging Research Postdoctoral Fellowship for Translational Research on Aging (M.X.). We thank M. Ruan, G.L. Evans, B.S. Thicke, and J.M. Peterson (Mayo Clinic) for their technical assistance. We also thank A.R. Thoreson, A.W. Hooke (Mayo Clinic), and the Mayo Clinic Materials and Structural Testing Resource Laboratory for performing the bone biomechanical compression and nano-indentation testing.

AUTHOR CONTRIBUTIONS

J.N.F. performed most of the experiments and analyses on *INK-ATTAC* and D + Q-treated mice. M.X. generated conditioned medium and defined the SASP mechanism. M.M.W. performed osteoclast cell culture experiments. M.X. and M.M.W. performed most of the experiments and analyses on JAKi-treated mice. D.G.M. provided technical guidance. D.G.F., J.L.O., B.A.N., J.G.S., M.B.O., C.M.H., T.P., T.T., N.K.L., M.T.D., R.J.P., and M.J.O. assisted with various aspects of the

experiments and analyses. J.N.F., M.X., M.M.W., T.T., J.L.K., and S.K. contributed to the design of experiments. J.N.F., M.W., and S.K. wrote the manuscript with input from all co-authors. S.K. directed and supervised all aspects of the study in collaboration with J.L.K. All authors reviewed the manuscript.

COMPETING FINANCIAL INTERESTS

The authors declare competing financial interests: details are available in the [online version of the paper](#).

Reprints and permissions information is available online at <http://www.nature.com/reprints/index.html>. Publisher's note: Springer Nature remains neutral with regard to jurisdictional claims in published maps and institutional affiliations.

1. Tchkonina, T., Zhu, Y., van Deursen, J., Campisi, J. & Kirkland, J.L. Cellular senescence and the senescent secretory phenotype: therapeutic opportunities. *J. Clin. Invest.* **123**, 966–972 (2013).
2. Baker, D.J. *et al.* Clearance of p16Ink4a-positive senescent cells delays ageing-associated disorders. *Nature* **479**, 232–236 (2011).
3. Xu, M. *et al.* Targeting senescent cells enhances adipogenesis and metabolic function in old age. *eLife* **4**, e12997 (2015).
4. Roos, C.M. *et al.* Chronic senolytic treatment alleviates established vasomotor dysfunction in aged or atherosclerotic mice. *Aging Cell* **15**, 973–977 (2016).
5. Zhu, Y. *et al.* The Achilles' heel of senescent cells: from transcriptome to senolytic drugs. *Aging Cell* **14**, 644–658 (2015).
6. Kirkland, J.L. & Tchkonina, T. Clinical strategies and animal models for developing senolytic agents. *Exp. Gerontol.* **68**, 19–25 (2015).
7. Xu, M. *et al.* JAK inhibition alleviates the cellular senescence-associated secretory phenotype and frailty in old age. *Proc. Natl. Acad. Sci. USA* **112**, E6301–E6310 (2015).
8. LeBrasseur, N.K., Tchkonina, T. & Kirkland, J.L. Cellular senescence and the biology of aging, disease, and frailty. *Nestle Nutr. Inst. Workshop Ser.* **83**, 11–18 (2015).
9. Swanson, E.C., Manning, B., Zhang, H. & Lawrence, J.B. Higher-order unfolding of satellite heterochromatin is a consistent and early event in cell senescence. *J. Cell Biol.* **203**, 929–942 (2013).
10. Zhu, Y., Armstrong, J.L., Tchkonina, T. & Kirkland, J.L. Cellular senescence and the senescent secretory phenotype in age-related chronic diseases. *Curr. Opin. Clin. Nutr. Metab. Care* **17**, 324–328 (2014).
11. Campisi, J. & d'Adda di Fagnano, F. Cellular senescence: when bad things happen to good cells. *Nat. Rev. Mol. Cell Biol.* **8**, 729–740 (2007).
12. Campisi, J. Senescent cells, tumor suppression, and organismal aging: good citizens, bad neighbors. *Cell* **120**, 513–522 (2005).
13. Jurk, D. *et al.* Postmitotic neurons develop a p21-dependent senescence-like phenotype driven by a DNA damage response. *Aging Cell* **11**, 996–1004 (2012).
14. Jurk, D. *et al.* Chronic inflammation induces telomere dysfunction and accelerates ageing in mice. *Nat. Commun.* **5**, 4172 (2014).
15. Minamino, T. *et al.* A crucial role for adipose tissue p53 in the regulation of insulin resistance. *Nat. Med.* **15**, 1082–1087 (2009).
16. Farr, J.N. *et al.* Identification of senescent cells in the bone microenvironment. *J. Bone Miner. Res.* **31**, 1920–1929 (2016).
17. Wang, E. Senescent human fibroblasts resist programmed cell death, and failure to suppress bcl2 is involved. *Cancer Res.* **55**, 2284–2292 (1995).
18. Nelson, G. *et al.* A senescent cell bystander effect: senescence-induced senescence. *Aging Cell* **11**, 345–349 (2012).
19. Coppé, J.P., Desprez, P.Y., Krtolica, A. & Campisi, J. The senescence-associated secretory phenotype: the dark side of tumor suppression. *Annu. Rev. Pathol.* **5**, 99–118 (2010).
20. Acosta, J.C. *et al.* A complex secretory program orchestrated by the inflammasome controls paracrine senescence. *Nat. Cell Biol.* **15**, 978–990 (2013).
21. Herbig, U., Ferreira, M., Condel, L., Carey, D. & Sedivy, J.M. Cellular senescence in aging primates. *Science* **311**, 1257 (2006).
22. Hamrick, M.W. *et al.* Age-related loss of muscle mass and bone strength in mice is associated with a decline in physical activity and serum leptin. *Bone* **39**, 845–853 (2006).
23. Glatt, V., Canalis, E., Stadmeier, L. & Bouxsein, M.L. Age-related changes in trabecular architecture differ in female and male C57BL/6J mice. *J. Bone Miner. Res.* **22**, 1197–1207 (2007).
24. Silva, M.J., Brodt, M.D. & Uthgenannt, B.A. Morphological and mechanical properties of caudal vertebrae in the SAMP6 mouse model of senile osteoporosis. *Bone* **35**, 425–431 (2004).
25. Oliver, W.C. & Pharr, G.M. An improved technique for determining hardness and elastic modulus using load and displacement sensing indentation experiments. *J. Mater. Res.* **7**, 1564–1583 (1992).
26. McGee-Lawrence, M.E. *et al.* Histone deacetylase 3 is required for maintenance of bone mass during aging. *Bone* **52**, 296–307 (2013).
27. Qing, H. *et al.* Demonstration of osteocytic perilacunar/canalicular remodeling in mice during lactation. *J. Bone Miner. Res.* **27**, 1018–1029 (2012).
28. Yi, J.-S. *et al.* Low-dose dasatinib rescues cardiac function in Noonan syndrome. *JCI Insight* **1**, e90220 (2016).

29. D'Andrea, G. Quercetin: A flavonol with multifaceted therapeutic applications? *Fitoterapia* **106**, 256–271 (2015).
30. Arai, F. *et al.* Commitment and differentiation of osteoclast precursor cells by the sequential expression of c-Fms and receptor activator of nuclear factor kappaB (RANK) receptors. *J. Exp. Med.* **190**, 1741–1754 (1999).
31. Bellido, T. *et al.* Regulation of interleukin-6, osteoclastogenesis, and bone mass by androgens. The role of the androgen receptor. *J. Clin. Invest.* **95**, 2886–2895 (1995).
32. Bendre, M.S. *et al.* Interleukin-8 stimulation of osteoclastogenesis and bone resorption is a mechanism for the increased osteolysis of metastatic bone disease. *Bone* **33**, 28–37 (2003).
33. Daci, E., Verstuyf, A., Moermans, K., Bouillon, R. & Carmeliet, G. Mice lacking the plasminogen activator inhibitor 1 are protected from trabecular bone loss induced by estrogen deficiency. *J. Bone Miner. Res.* **15**, 1510–1516 (2000).
34. Khosla, S. Odanacatib: location and timing are everything. *J. Bone Miner. Res.* **27**, 506–508 (2012).
35. Mullard, A. Merck & Co. drops osteoporosis drug odanacatib. *Nat. Rev. Drug Discov.* **15**, 669 (2016).
36. Lyles, K.W. *et al.* Zoledronic acid and clinical fractures and mortality after hip fracture. *N. Engl. J. Med.* **357**, 1799–1809 (2007).
37. Zhu, Y. *et al.* Identification of a novel senolytic agent, navitoclax, targeting the Bcl-2 family of anti-apoptotic factors. *Aging Cell* **15**, 428–435 (2016).
38. Wright, N.C. *et al.* The recent prevalence of osteoporosis and low bone mass in the United States based on bone mineral density at the femoral neck or lumbar spine. *J. Bone Miner. Res.* **29**, 2520–2526 (2014).
39. Burge, R. *et al.* Incidence and economic burden of osteoporosis-related fractures in the United States, 2005–2025. *J. Bone Miner. Res.* **22**, 465–475 (2007).

ONLINE METHODS

General experimental approaches. No samples, mice or data points were excluded from the reported analyses. Animals were randomized to experimental groups, as indicated below. Analyses were performed in a blinded fashion, as noted below. Detailed information on experimental design and reagents is available through the accompanying **Life Sciences Reporting Summary**.

Mouse strains and drug treatments. Mice were housed in ventilated cages and maintained within a pathogen-free, accredited facility under a 12-h light–dark cycle with constant temperature (23 °C) and access to food (standard mouse diet, Lab Diet 5053, St. Louis, MO) and water *ad libitum*. All animal protocols were approved by the Institutional Animal Care and Use Committee (IACUC), and all experiments were performed in accordance with IACUC guidelines. Both sexes were studied as specified below and in the figure legends.

The generation and characterization of the *INK-ATTAC* transgenic mouse line has been described². Based on the original idea and initial experimental strategies devised by J.L.K. and T.T., *INK-ATTAC* mice were co-developed by the Kirkland and J. van Deursen (Mayo) laboratories and bred onto a C57BL/6 background in the van Deursen laboratory, and then the Kirkland laboratory genotyped them to select *INK-ATTAC* heterozygotes and let them age to 6–12 (young) or 20 (old) months. All experiments using the *INK-ATTAC* mice were performed on transgenic line 3, which contains 13 copies of the transgene, inserted into a single locus². Female *INK-ATTAC* mice from this cohort were randomly assigned to be injected (intraperitoneally (i.p.)) with vehicle or AP20187 (B/B homodimerizer, Clontech; 10 mg of AP20187 per kg body mass (drug/body mass)) twice weekly, beginning at 20 months of age for a total of 4 months (all old mice were killed at 24 months of age). This dosing regimen was chosen because it was effective at clearing senescent cells in chronologically aged old *INK-ATTAC* mice in previous studies^{3,4}. Young (12-month-old) female *INK-ATTAC* mice were treated using the same dosing regimen for 1.5 months (killed at 13.5 months of age). In addition, from a previous study in the Kirkland laboratory in which no bones were harvested, we obtained plasma samples from young (6-month-old) female *INK-ATTAC* mice that were treated using the same dosing regimen for 4 months.

C57BL/6 male mice were obtained from the National Institute on Aging (NIA) at 7, 20 or 22 months of age. Alternatively, C57BL/6 breeding colonies were maintained to generate animals for *in vitro* osteoclastogenesis assays. 20-month-old male C57BL/6 mice were randomly assigned to once monthly treatments by oral gavage with dasatinib and quercetin (D + Q) or vehicle for 4 months⁵. In pilot studies, weekly and biweekly D + Q were also evaluated, with similar effects to once monthly dosing. The once-monthly dosing regimen was chosen to avoid potential off-target effects and because it was effective at clearing senescent cells in a previous cohort of old mice⁴. D and Q were diluted in 10% PEG400 and delivered by oral gavage at dosages of 5 mg/kg and 50 mg/kg, respectively, in 100 μ l.

7-month-old (young) or 22-month-old (old) male C57BL/6 mice were randomly assigned to treatment with either the JAK 1/2 inhibitor, ruxolitinib (JAKi), or vehicle for 2 months (mice were killed at 9 months (young) or 24 months (old) of age), as part of a previously published study⁷. JAKi was dissolved in DMSO and mixed with chow. DMSO (vehicle) chow or JAKi chow was administered daily (0.5 g per animal) for 2 months at a dose of 60 mg/kg (drug/body mass). This dosing regimen was effective at blocking the SASP in old mice⁷.

Note that whereas female mice were used in the *INK-ATTAC* study, on the basis of availability from the National Institute on Aging mouse colony, male mice were used in the senolytic and JAK-inhibitor studies.

Tissue collection. Mice were killed, body mass was recorded and serum/plasma was collected via cardiac puncture at time of death and stored at –80 °C. The right femur/tibia and lumbar vertebrae were fixed in 10% neutral buffered formalin and stored in ethanol to be used for microcomputed tomography (μ CT), histomorphometry and SADS). The remaining vertebrae were used for osteocyte-enriched cell isolations. The tail was collected at the base and stored in PBS-soaked gauze at –20 °C for biomechanical compression and biomaterial nanoindentation testing of the caudal vertebrae. For *in vitro* analyses of osteoclast progenitors or osteoclastogenesis, left femurs/tibiae were isolated and dissected free of soft tissue, epiphyses were removed and marrow

was flushed with PBS. As described⁷, perigonadal adipose tissue was collected and either fixed (for SA- β -gal staining) or snap-frozen in liquid nitrogen for RNA and subsequent RT–qPCR analyses.

Isolation of osteocyte-enriched cells. Detailed methods and validation of our osteocyte-enriched cell isolation protocol are presented elsewhere^{16,27}. Briefly, mouse vertebrae were stripped of muscle and connective tissues, minced and sequentially digested twice for 30-min in collagenase (Liberase; Roche Diagnostics GmbH, Mannheim, Germany). As shown previously¹⁶, the remaining cell fraction represents a highly enriched population of osteocytes used for RT–qPCR analyses.

SADS analysis of senescent osteocytes. SADS⁹ was measured *in vivo* in a blinded fashion, as described¹⁶, in osteocytes located in cortical bone in the long bone diaphyses. Briefly, the decalcified right tibiae of mice were fixed, embedded in methylmethacrylate (MMA), and sectioned, which was followed by fluorescence *in situ* hybridization (FISH)¹⁶. Bone sections were cross-linked with 4% paraformaldehyde (PFA) for 20 min, washed three times in PBS (5 min each), and dehydrated in graded ethanol as follows: 70%, 90%, and 100% (3 min each). Following a brief air drying, sections were denatured for 10 min at 80 °C in hybridization buffer: 70% formamide (Sigma-Aldrich), 25-mM MgCl₂, 0.1-M Tris (pH 7.2), 5% blocking reagent (Roche) containing 1.0 μ g/ml of Cy3-labeled (F3002, reacts to both human and mouse), and CENPB-specific (ATTCGTTGGAAACGGGA) peptide nucleic acid (PNA) FISH probe (Panagene, South Korea), which was followed by hybridization for 2 h at room temperature in the dark. Slides were washed, stained, and mounted with vectashield DAPI-containing mounting media (Life Technologies). In addition, we performed the SADS assay on primary murine osteocytes isolated from long-bone diaphyses using the Bonewald Laboratory technique⁴⁰; cells were either untreated or treated with 10 Gy of cesium irradiation (to induce senescence) and cultured in a humidified incubator (maintained at 37 °C and 5% CO₂) for 20 d. SADS were visualized using confocal microscopy (Mayo Clinic Microscopy and Cell Analysis Core) as described¹⁶. The numbers of decondensed/elongated centromeres per osteocyte were quantified, as described¹⁶. We previously established a cut-off for defining cell senescence as ≥ 4 SADS per cell¹⁶.

Senescence-associated β -galactosidase (SA- β -gal) assay. Cellular SA- β -gal activity was measured to detect lysosomes in senescent cells⁴¹. Detailed methods for the SA- β -gal assay have been previously described⁷. Briefly, perigonadal adipose tissue samples or primary murine osteocytes were fixed with 2% (vol/vol) formaldehyde (Sigma-Aldrich) and 25% glutaraldehyde (Sigma-Aldrich) in PBS for 5 min. After washing with PBS three times, samples were incubated in SA- β -gal solution (pH 6.0) at 37 °C for 16–18 h. Ice-cold PBS was then used to stop the enzymatic reaction. In blinded analyses, for each sample, ten images were taken from random fields using Fluorescence Microscopy (Nikon Eclipse Ti). DAPI (Life Technologies) was used to stain nuclei for cell counting.

Skeletal phenotyping. All imaging was performed in a blinded fashion. Areal bone mineral density (aBMD; g/cm²) of the lumbar spine (L₁–L₄) was measured by dual-energy X-ray absorptiometry (DXA) using a Lunar PIXImus densitometer (software version 1.44.005; Lunar Corp., Madison, WI)⁴². Measures of total (metaphysis), trabecular (metaphysis), and cortical (midshaft diaphysis) volumetric BMD (vBMD; mg/cm³) at the tibia were obtained using peripheral quantitative computed tomography (pQCT; Stratec XCT Research SA Plus, software v5.40, Nordland Medical Systems, Fort Atkinson, WI)⁴². Quantitative analysis of the lumbar spine (L₄–L₆) and distal femoral metaphysis were performed using the Viva Scan 40 μ CT scanner (Scanco Medical AG, Basserdorf, Switzerland) with the following parameters: 55 kVp, 145 mA, high resolution, 21.5 diameter, 10.5- μ m voxel size, 300-ms integration time. Using two-dimensional (2D) data from scanned slices, 3D analysis was used to calculate morphometric parameters at both the lumbar spine (200 slices) and distal femoral metaphysis (100 slices) defining trabecular bone mass and microarchitecture, including trabecular bone volume fraction (BV/TV; %), trabecular number (Tb.N; 1/mm), trabecular thickness (Tb.Th; mm), trabecular

separation (Tb.Sp; mm; higher values are associated with weaker bone), and the SMI, which indicates whether trabeculae are stronger and plate-like (lower values) or weaker and rod-like (higher values). Cortical thickness (Ct.Th; mm) was assessed at the distal femoral metaphysis (50 slices). Microfinite element analysis (μ FEA) was performed at the femoral metaphysis to assess failure load (N; i.e., bone strength) using the manufacturer's software (Scanco Medical AG, Basserdorf, Switzerland; Finite Element-Software Version 1.13). All μ CT parameters were derived using the manufacturer's protocols.

Compression loading. Loading tests were performed in a blinded fashion. The sixth caudal vertebrae (Ca6) was removed from the tail, stripped of soft tissue, and measured end-to-end with a digital caliper (ABSOLUTE, Mitutoyo, Aurora, IL). Vertebrae were soaked in PBS for 15–30 min before testing to ensure hydration. Cyanoacrylate adhesive was applied to each end of the bones to mount them between two #10-32 stainless steel nuts filled with PMMA resin. The assembly was loaded into an alignment guide to impart parallel loading surfaces at each end of the bone while the adhesive cured for 5 min. Compression testing was conducted with a servohydraulic test system instrumented with a 450-Newton (N) capacity load cell (Mini Bionix II, MTS Systems, Eden Prairie, MN). Bones were pre-loaded to 1 N and then loaded until failure under displacement control at a rate of 0.02 mm/s, as previously described²⁴. Force and displacement data were collected at a sample rate of 100 Hz. The yield load (N), ultimate load (N), ultimate displacement (mm), and energy to ultimate failure (mJ) were evaluated.

Nano-indentation. Nano-indentation was performed in a blinded fashion. The seventh caudal vertebra (Ca7) was removed from the tail and stripped of soft tissue. Specimens were embedded in PMMA resin (Lecocet 100, Leco, St. Joseph, MO) and then sectioned transversely within the body of the vertebrae with a low-speed diamond saw (Isomet, Buehler, Lake Bluff, IL). Sections were manually polished with a polishing/grinding system (Ecomet 250, Buehler) using successively finer abrasive cloths (400, 600, 800, and 1200 grit) with a final polish using a microcloth and slurry of 0.05- μ m aluminum abrasive (Union Carbide, Houston, TX). Indentation testing was conducted on cortical bone with a nano-indentation system (TI 950, Hysitron, Minneapolis, MN) equipped with a diamond Berkovich pyramidal tip. Four sites, widely distributed around cross-section, were tested on each bone. At each site, a 2×2 array was indented with 15- μ m spacing between indents. Indentation was conducted under load control at a rate of 500 μ N/s to a peak load of 2,000 μ N with a 60-s hold before unloading to reduce viscoelastic effects, as previously described²⁶. The reduced modulus (E_r ; GPa), and hardness (H ; GPa), were calculated using the Oliver–Pharr model, as previously described²⁵. Measures were averaged over the four indents of the array to generate a value for the site. Values obtained at the four sites were averaged to generate an aggregate value for each specimen.

Histomorphometric analyses. All histomorphometric analyses were performed in a blinded fashion. For dynamic histomorphometric analyses, mice were injected subcutaneously with Alizarin Red (0.1 ml/animal, 7.5 mg/ml) and calcein (0.1 ml/animal, 2.5 mg/ml) on days 9 and 2, respectively, before euthanasia. The lumbar vertebrae and right femur were isolated from female *INK-ATTAC* mice treated with vehicle or AP20187 or male C57BL/6 mice treated with vehicle or D + Q and were embedded in MMA, sectioned, and stained with Masson Trichrome to assess osteoblast numbers per bone perimeter (N.Ob/B.Pm, /mm), or stained for TRAP activity to assess osteoclast numbers per bone perimeter, N.Oc/B.Pm, /mm). Alternatively, sections were left unstained to quantify mineralizing surfaces (mineral apposition rate, MAR, mcm/d; bone formation rate per bone surface, BFR/BS, mcm³/mcm²/d). Femurs obtained from vehicle- or JAKi-treated C57BL/6 male mice were decalcified for 2 weeks in 12.5% EDTA, followed by paraffin embedding, sectioning, and staining with Goldner's Trichrome stain. Osteoblast (N.Ob/B.Pm) and osteoclast (N.Oc/B.Pm) numbers were assessed. The determination of bone marrow adipocyte parameters has been described by our group previously⁴². Briefly, adipocyte number, adipocyte perimeter (mm), and adipocyte volume per tissue volume were measured by tracing out individual adipocytes in all the fields analyzed. All histomorphometric measurements and

calculations were performed with the Osteomeasure Analysis system (Osteometrics, Atlanta, Georgia).

Real-time quantitative polymerase chain reaction (RT-qPCR) analyses. Targeted gene expression analyses were performed by RT-qPCR as described¹⁶. Briefly, total RNA was isolated using QIAzol Lysis Reagent and RNeasy Mini Columns (QIAGEN, Valencia, CA). DNase treatment was applied to degrade contaminating genomic DNA using an on-column RNase-free DNase solution (QIAGEN, Valencia, CA). RNA quantity and purity were confirmed with a Nanodrop spectrophotometer (Thermo Scientific, Wilmington, DE). Reverse transcriptase was performed using the High-Capacity cDNA Reverse Transcription Kit (Applied Biosystems by Life Technologies, Foster City, CA). PCR reactions were run using the ABI Prism 7900HT Real Time System (Applied Biosystems, Carlsbad, CA) with either SYBR green (QIAGEN, Valencia, CA) or TaqMan (Applied Biosystems, Carlsbad, CA). Note that TaqMan assays (purchased from Thermo Fisher Scientific) were used to measure *p16^{Ink4a}* (*Cdkn2a*), *EGFP*, *Sost*, *Opg* (*Tnfrsf11b*), and *Rankl* (*Tnfrsf11*) (normalized to *Tbp* or *Actb*), whereas all other genes (normalized to *Tuba1*) were measured using SYBR green. Murine primers for *Trap* (*Acp5*), *Cathepsin K* (*Ctsk*), *Oscar*, *Oc-stamp*, and *Tnfrsf11a* (*Rank*) were designed using Primer Express[®] Software Version 3.0 (Applied Biosystems, Foster City, CA) according to the following forward and reverse pair sequences:

Acp5: forward 5'-CGCTTCAAAATTCACGTACAA-3' & reverse 5'-CAGCATCACTGTGTCCAGCAT-3'; *Ctsk*: forward 5'-GGATGAAATCTCTCGGC GTTT-3' & reverse 5'-GGTTATGGGCAGAGATTGCTT-3'; *Oscar*: forward 5'-CTCTTCAAAAGTGGCCTTGTC-3' & reverse 5'-GGAAGAAGCTCAGCC AGCTCAA-3'; *Oc-stamp*: forward 5'-TGAGCCTGGGCTCAGAAAGT-3' & reverse 5'-GTTGGTTGAGGACGAAGAGG-3'; *Tnfrsf11a*: forward 5'-ACTGA GGAGACCACCAAGGA-3' & reverse 5'-TGAAGAGGAGCAGAACGATGAG-3'.

Conditioned medium generation. Subcutaneous adipose tissue samples were collected from healthy, lean (BMI 26.6 ± 0.9 kg/m²) kidney donors aged 39 ± 3.3 years for isolation of primary human adipose-derived mesenchymal stem cells (AdMSCs) as described⁴³. The protocol was approved by the Mayo Foundation Institutional Review Board informed consent was obtained from all human subjects. Cellular senescence was induced in AdMSCs by 10 Gy of cesium irradiation as described⁷. JAK inhibitor 1 (CAS 457081-03-7) was purchased from EMD Millipore (Billerica, MA). Ruxolitinib (INCB18424, CAS 941678-49-5) was purchased from ChemieTek (Indianapolis, IN). Conditioned medium (CM) was made of RPMI 1640 containing 1-mM sodium pyruvate, 2-mM glutamine, MEM vitamins, MEM nonessential amino acids, and antibiotic (Thermo Fisher Scientific). For collection, human nonproliferating control (CON) or senescent (SEN) AdMSCs cells were washed three times with PBS and cultured in CM for 24 h. For JAK inhibitor treatment, cells were treated with 0.6- μ M JAK inhibitor 1 or DMSO in α -MEM containing 10% FBS and antibiotic for 48 h. Cells were then washed three times with PBS and exposed to media containing JAK inhibitor or DMSO for another 24 h.

In vitro osteoblast differentiation. MC3T3-E1 (subclone 4) cells were plated at a density of 1×10^4 cells per cm² in α -MEM without ascorbic acid. After reaching confluency (~48 h), media was replaced and cells were cultured for an additional 72 h. Differentiation media consisted of α -MEM containing ascorbic acid with the addition of 50 μ g/ml ascorbic acid and 10-mM β -glycerolphosphate. Cells were cultured in the presence of 20% control or senescent CM. Differentiation media and CM treatments were replaced every 3 or 4 d until day 21. Cells were fixed with 1% PFA, and stained with Alizarin Red S (Sigma-Aldrich) to assess osteoblast mineralization. Cultures were stained for 15 min, washed with H₂O, and dried before obtaining images. Alizarin Red stain was eluted with 10% cetylpyridinium chloride in NaP buffer and absorbance was assessed at 540 nm.

Osteoclast differentiation and quantification. Following euthanasia, long bones were isolated from C57BL/6 mice, 5–8 weeks of age. As described above, bone marrow was flushed with sterile PBS. Red blood cells (RBCs) were lysed using RBC lysis buffer ($1 \times$) (eBioscience, San Diego, CA), and marrow counts were obtained. Equal cell numbers were cultured overnight in vehicle (negative

control), 25 ng/ml rmM-CSF (positive control) (R&D Systems, Minneapolis, MN), control CM, senescent CM, or CM from senescent cells treated with the JAK inhibitor 1 (SEN/JAKi). CM treatments were 1:1 with α -Minimal Essential Medium (MEM, Invitrogen, Carlsbad, CA) with 10% FBS (FBS) and 1 \times antibiotic/antimycotic. Negative and positive controls were 1:1 with control RPMI 1640 used for AdMSC culture. As a control for the presence of the JAK inhibitor 1, cells were treated with control CM or senescent CM with the addition of freshly added vehicle (DMSO) or JAK inhibitor 1 (0.3- μ M final concentration). The nonadherent populations were collected 24 h after plating. Cell counts were obtained, and viability was assessed with Trypan Blue. Equal cell numbers were then plated in osteoclast differentiation medium (α -MEM) with 10% FBS, 1 \times antibiotic/antimycotic, 1:50 CMB 14-12 supernatant (source of M-CSF⁴⁴) and 200 ng/ml mouse receptor activator of NF- κ B ligand (RANKL)-GST (generated using a recombinant RANKL expression construct provided by B. Lee, Ohio State University)). Osteoclast differentiation was carried out for 2–4 d, with differentiation media replaced on day 3. Mature osteoclasts formed on days 3 and 4.

Alternatively, mouse monocytes were isolated from mouse bone marrow by negative selection using the Mouse Monocyte Isolation Kit (Miltenyi Biotec, San Diego, CA) and magnetic activated cell sorting (MACS, autoMACS-Pro magnetic cell sorter, Miltenyi Biotec, Inc.). Monocytes were cultured with CON or SEN CM overnight, as described above. Nonadherent populations were collected, counted, and plated at equal cell densities in osteoclast differentiation medium.

To assess osteoclastogenesis in vehicle or ruxolitinib (JAKi) treated mice, RBC-lysed marrow was plated directly in osteoclast differentiation medium. Osteoclast differentiation medium was replaced on day 3 and osteoclast cultures were fixed on day 4.

Mature osteoclast cultures were fixed in 1% PFA and osteoclast differentiation was assessed by TRAP activity (Acid Phosphatase, Leukocyte Kit, Sigma-Aldrich, St. Louis, MO)⁴⁵. Osteoclasts were defined as TRAP-positive cells with greater than three nuclei.

Flow cytometry. Whole bone marrow was cultured overnight with CON or SEN CM as described above. The nonadherent cells were collected and counted. For each sample, 5 μ L Fc Blocking Reagent was added to 1 \times 10⁶ cells in FACS buffer, and cells were stained with APC-conjugated anti-CD115 (eBioscience) and PE-conjugated anti-RANK (ThermoFisher) in a total volume of 100 μ L. Cells were washed and fixed with 1% PFA. Cells were sorted using FACSCalibur (BD Biosciences), and data were analyzed by FlowJo (FlowJo, LLC); gates were set according to unstained and single label controls for APC and PE, respectively.

Apoptosis. Apoptosis was assessed using ApoTox-Glo Triplex Assay (Promega, Madison, WI). Bone marrow or monocyte-enriched cultures (Mouse Monocyte Isolation Kit, Miltenyi Biotec) were treated for 24 h with CON or SEN CM, and apoptosis was quantified. Alternatively, bone marrow was differentiated for 4 d into mature osteoclasts as described above. On day 4, mature osteoclast cultures were treated with vehicle or 10-nM AP20187 (the same *in vitro* dose used previously²) in fresh osteoclast differentiation media. Cells were incubated for 18 h followed by apoptosis quantification. Briefly, a luminogenic caspase-3/7 substrate was added to cells. Cultures were incubated for 30 min at RT, and luminescence was measured using the GloMax-Multi Detection System (Promega).

MethoCult assay. Bone marrow was plated in MethoCult GF 3434 Media (StemCell Technologies, Vancouver, BC, Canada). Each mouse was tested in duplicate. Cultures were incubated for 10 d and colonies were identified as monocyte/macrophage (M) or granulocyte-monocyte/macrophage (GM).

Colony-forming units (CFU)-M and CFU-GM per plate were counted and averaged per mouse. Analyses were done in a blinded fashion.

Serum/plasma assays. Peripheral blood for serum/plasma measurements was collected from overnight fasted mice by cardiac puncture; samples were stored at -80 °C in aliquots. Circulating plasma C-terminal telopeptide of type I collagen (CTx) levels in young and old *INK-ATTAC* mice were measured by enzyme immunoassay (EIA) (Immunodiagnostic Systems). Serum IL-6 and CXCL1 (IL-8) levels in JAKi-treated mice were previously measured⁷ using Luminex xMAP technology. Mouse ELISA kits (R&D Systems) were used to measure circulating plasma levels of IL-6, CXCL1 (mouse homolog to IL-8), and PAI-1 in all the other mice in **Supplementary Figure 14**. All assays were performed in a blinded fashion.

Cell-line identity. MC3T3-E1 (subclone 4) cells were obtained from the ATCC (ATCC CRL-2593) to assess the effects of senescent CM on osteoblast differentiation. This cell line is not listed in the database of commonly misidentified cell lines maintained by ICLAC. Given that these cells were freshly obtained from the ATCC, we did not perform testing for mycoplasma contamination. All other experiments were performed with primary cells.

Reagents. Antibodies and other reagents were purchased from commercial sources; details are available from vendors as indicated throughout the Methods.

Statistical analyses. Sample sizes were based on pilot or previously conducted and published experiments (for example, Syed *et al.*⁴²), in which statistically significant differences were observed on bone with various interventions in our laboratory. For each experiment, replicates are as noted in the figure legends. No samples were excluded from analyses. Investigators were blinded to allocation during experiments and outcome assessments, as noted specifically above. Data were checked for normality using histograms and all variables were tested for skewness and kurtosis. Analyses of differences between groups were performed by independent samples *t*-test, Wilcoxon rank-sum tests, one-way ANOVA, or repeated-measures ANOVA where justified as appropriate (see figure legends). Following ANOVA, the Bonferroni *post hoc* test was used to adjust for multiple comparisons. Data are presented as means \pm s.e.m. (unless otherwise specified) with *P* < 0.05 (two-tailed) considered to be statistically significant. Statistical analyses were performed using the Statistical Package for the Social Sciences for Windows, Version 22.0 (SPSS, Chicago, IL).

Data availability. Data presented in this manuscript are available from the corresponding authors upon reasonable request. Source data are available for **Figures 1–4**.

40. Stern, A.R. *et al.* Isolation and culture of primary osteocytes from the long bones of skeletally mature and aged mice. *Biotechniques* **52**, 361–373 (2012).
41. Lee, B.Y. *et al.* Senescence-associated beta-galactosidase is lysosomal beta-galactosidase. *Aging Cell* **5**, 187–195 (2006).
42. Syed, F.A. *et al.* Skeletal effects of estrogen are mediated by opposing actions of classical and nonclassical estrogen receptor pathways. *J. Bone Miner. Res.* **20**, 1992–2001 (2005).
43. Tchkonian, T. *et al.* Abundance of two human preadipocyte subtypes with distinct capacities for replication, adipogenesis, and apoptosis varies among fat depots. *Am. J. Physiol. Endocrinol. Metab.* **288**, E267–E277 (2005).
44. Takeshita, S., Kaji, K. & Kudo, A. Identification and characterization of the new osteoclast progenitor with macrophage phenotypes being able to differentiate into mature osteoclasts. *J. Bone Miner. Res.* **15**, 1477–1488 (2000).
45. Gingery, A., Bradley, E., Shaw, A. & Oursler, M.J. Phosphatidylinositol 3-kinase coordinately activates the MEK/ERK and AKT/NF κ B pathways to maintain osteoclast survival. *J. Cell. Biochem.* **89**, 165–179 (2003).

Corrigendum: Host DNA released by NETosis promotes rhinovirus-induced type-2 allergic asthma exacerbation

Marie Toussaint, David J Jackson, Dawid Swieboda, Anabel Guedán, Theodora-Dorita Tsourouktsoglou, Yee Man Ching, Coraline Radermecker, Heidi Makrinioti, Julia Aniscenko, Michael R Edwards, Roberto Solari, Frédéric Farnir, Venizelos Papayannopoulos, Fabrice Bureau, Thomas Marichal & Sebastian L Johnston
Nat. Med. 23, 681–691 (2017); published online 1 May 2017; corrected after print 12 July 2017

In the version of this article initially published, Dr. Nathan W Bartlett was inadvertently omitted from the author list and the Contributions section. The errors have been corrected in the HTML and PDF versions of the article.

Corrigendum: The cold-induced lipokine 12,13-diHOME promotes fatty acid transport into brown adipose tissue

Matthew D Lynes, Luiz O Leiria, Morten Lundh, Alexander Bartelt, Farnaz Shamsi, Tian Lian Huang, Hirokazu Takahashi, Michael F Hirshman, Christian Schlein, Alexandra Lee, Lisa A Baer, Francis J May, Fei Gao, Niven R Narain, Emily Y Chen, Michael A Kiebish, Aaron M Cypess, Matthias Blüher, Laurie J Goodyear, Gökhan S Hotamisligil, Kristin I Stanford & Yu-Hua Tseng
Nat. Med. 23, 631–637 (2017); published online 27 March 2017; corrected after print 23 August 2017

In the phrase, “Here we show that the lipid 12,13-dihydroxy-9Z-octadecenoic acid (12,13-diHOME) is a stimulator of BAT activity, and that its levels are negatively correlated with body-mass index and insulin sensitivity,” located in the abstract, the word “resistance” should take the place of the word “sensitivity”.

Also, the authors have clarified in more detail how the FATP1 oligomer density was quantitated in Figure 4f. This information can be found in the “Membrane Fractionation” section of the Online Methods: “To quantify FATP1 in scanned immunoblots, regions of interest of identical size were drawn in each lane at the same molecular weight, and integrated pixel density was measured using ImageJ software. For each independent experimental replicate, the integrated pixel density for each lane was expressed normalized to the control lane, or in the case of the experimental replicate with two control lanes, the integrated pixel density for each lane was expressed normalized to the average of both control lanes. The data are expressed as the average normalized value for each lane, with the error bars representing s.e.m.”

Corrigendum: Targeting cellular senescence prevents age-related bone loss in mice

Joshua N Farr, Ming Xu, Megan M Weivoda, David G Monroe, Daniel G Fraser, Jennifer L Onken, Brittany A Negley, Jad G Sfeir, Mikolaj B Ogrodnik, Christine M Hachfeld, Nathan K LeBrasseur, Matthew T Drake, Robert J Pignolo, Tamar Pirtskhalava, Tamara Tchkonina, Merry Jo Oursler, James L Kirkland & Sundeep Khosla
Nat. Med. 23, 1072–1079 (2017); published online 21 August 2017; corrected after print 11 October 2017

In the version of this article initially published, the representative images in Fig. 2n were inadvertently duplicated in Fig. 4h. A correct version of the images for Fig. 4h has been supplied. The authors wish to point out that this error did not affect the other data reported in the paper or the conclusions drawn. The error has been corrected in the HTML and PDF versions of the article.

Corrigendum: Genome-wide CRISPR screens reveal a Wnt–FZD5 signaling circuit as a druggable vulnerability of *RNF43*-mutant pancreatic tumors

Zachary Steinhart, Zvezdan Pavlovic, Megha Chandrashekhar, Traver Hart, Xiaowei Wang, Xiaoyu Zhang, Mélanie Robitaille, Kevin R Brown, Sridevi Jaksani, René Overmeer, Sylvia F Boj, Jarrett Adams, James Pan, Hans Clevers, Sachdev Sidhu, Jason Moffat & Stéphane Angers
Nat. Med. 23, 60–68 (2017); published online 21 November 2016; corrected after print 20 September 2017

In the version of this article initially published, duplicate panels in Figure 5e were incorrectly used in the assembly of the figure, for which all original panels are presented in Supplementary Figure 10. The errors in Figure 5e have been corrected in the HTML and PDF versions of the article.

Life Sciences Reporting Summary

Nature Research wishes to improve the reproducibility of the work that we publish. This form is intended for publication with all accepted life science papers and provides structure for consistency and transparency in reporting. Every life science submission will use this form; some list items might not apply to an individual manuscript, but all fields must be completed for clarity.

For further information on the points included in this form, see [Reporting Life Sciences Research](#). For further information on Nature Research policies, including our [data availability policy](#), see [Authors & Referees](#) and the [Editorial Policy Checklist](#).

► Experimental design

1. Sample size

Describe how sample size was determined.

Sample sizes were based on pilot or previously conducted and published experiments (e.g. J Bone Miner Res. 2005 Nov;20(11):1992-2001) in which statistically significant differences were observed on bone with various interventions in our laboratory.

2. Data exclusions

Describe any data exclusions.

No samples were excluded from analyses.

3. Replication

Describe whether the experimental findings were reliably reproduced.

No attempts at experimental replication failed.

4. Randomization

Describe how samples/organisms/participants were allocated into experimental groups.

For each study, all mice were randomly allocated into experimental groups.

5. Blinding

Describe whether the investigators were blinded to group allocation during data collection and/or analysis.

Investigators were blinded to allocation during experiments and outcome assessments (during both data collection and analysis), except for rare instances in which this was not possible.

Note: all studies involving animals and/or human research participants must disclose whether blinding and randomization were used.

6. Statistical parameters

For all figures and tables that use statistical methods, confirm that the following items are present in relevant figure legends (or in the Methods section if additional space is needed).

- | | |
|--------------------------|--|
| n/a | Confirmed |
| <input type="checkbox"/> | <input checked="" type="checkbox"/> The <u>exact sample size</u> (<i>n</i>) for each experimental group/condition, given as a discrete number and unit of measurement (animals, litters, cultures, etc.) |
| <input type="checkbox"/> | <input checked="" type="checkbox"/> A description of how samples were collected, noting whether measurements were taken from distinct samples or whether the same sample was measured repeatedly |
| <input type="checkbox"/> | <input checked="" type="checkbox"/> A statement indicating how many times each experiment was replicated |
| <input type="checkbox"/> | <input checked="" type="checkbox"/> The statistical test(s) used and whether they are one- or two-sided (note: only common tests should be described solely by name; more complex techniques should be described in the Methods section) |
| <input type="checkbox"/> | <input checked="" type="checkbox"/> A description of any assumptions or corrections, such as an adjustment for multiple comparisons |
| <input type="checkbox"/> | <input checked="" type="checkbox"/> The test results (e.g. <i>P</i> values) given as exact values whenever possible and with confidence intervals noted |
| <input type="checkbox"/> | <input checked="" type="checkbox"/> A clear description of statistics including <u>central tendency</u> (e.g. median, mean) and <u>variation</u> (e.g. standard deviation, interquartile range) |
| <input type="checkbox"/> | <input checked="" type="checkbox"/> Clearly defined error bars |

See the web collection on [statistics for biologists](#) for further resources and guidance.

► Software

Policy information about [availability of computer code](#)

7. Software

Describe the software used to analyze the data in this study.

Statistical analyses were performed using the Statistical Package for the Social Sciences for Windows, Version 22.0 (SPSS, Chicago, IL) or using GraphPad software (GraphPad Software, Inc., San Diego, CA, USA) (www.graphpad.com).

For manuscripts utilizing custom algorithms or software that are central to the paper but not yet described in the published literature, software must be made available to editors and reviewers upon request. We strongly encourage code deposition in a community repository (e.g. GitHub). *Nature Methods* [guidance for providing algorithms and software for publication](#) provides further information on this topic.

► Materials and reagents

Policy information about [availability of materials](#)

8. Materials availability

Indicate whether there are restrictions on availability of unique materials or if these materials are only available for distribution by a for-profit company.

No unique materials were used for this study.

9. Antibodies

Describe the antibodies used and how they were validated for use in the system under study (i.e. assay and species).

RANK Monoclonal Antibody, PE: (9A725), ThermoFisher Scientific, MA1-41015, lot# SC2353362A. Species reactivity: Mouse, Human. Manufacturer provided intracellular flow analysis in RAW cells using 0.5ug of antibody vs isotype control, demonstrating the specificity of this antibody. This antibody has previously been used for flow cytometry in the following publications: PMID 26329493, PMID 22531921. This antibody is also referenced in the Labome database of validated antibodies: <https://www.labome.com/product/Invitrogen/MA1-41015.html>
CD115 (CSF-1R) Antibody, APC: (AFS98) eBioscience, cat# 17-1152-82, lot# 4293537. Species reactivity: Mouse. Manufacturer provided intracellular flow analysis in peritoneal exudate cells using 0.03ug of antibody vs APC isotype control, demonstrating the specificity of this antibody. This antibody has been previously used in the following select publications: PMID 25503582, PMID 21654748. This antibody is also referenced in the Labome database of validated antibodies: <https://www.labome.com/product/Invitrogen/17-1152-82.html>.

10. Eukaryotic cell lines

- State the source of each eukaryotic cell line used.
- Describe the method of cell line authentication used.
- Report whether the cell lines were tested for mycoplasma contamination.
- If any of the cell lines used are listed in the database of commonly misidentified cell lines maintained by [ICLAC](#), provide a scientific rationale for their use.

MC3T3-E1 subclone 4 was obtained from ATCC (ATCC® CRL-2593™).

These cells were obtained and expanded directly from ATCC, within 30 days of receipt of the cell line. They exhibited mineralization activity consistent with what has been previously reported for this cell line.

As these cells were freshly obtained from ATCC, we did not perform testing for mycoplasma contamination.

MC3T3-E1 (subclone 4) cells were obtained from ATCC. This cell line is not listed in the database of commonly misidentified cell lines maintained by ICLAC.

► Animals and human research participants

Policy information about [studies involving animals](#); when reporting animal research, follow the [ARRIVE guidelines](#)

11. Description of research animals

Provide details on animals and/or animal-derived materials used in the study.

Both sexes of C57BL/6 mice (*Mus musculus*) were studied. Female INK-ATTAC heterozygotes on the C57BL/6 background were used between the ages of 6-13.5 months (young) or 20-24 months (old). Male C57BL/6 mice between the ages of 7-9 months (young) or 20-24 months (old) were used for D+Q and JAK inhibitor studies. In addition, young C57BL/6 male mice aged 5-8 weeks were utilized to test the effects of senescent cell conditioned media on osteoclastogenesis in vitro.

12. Description of human research participants

Describe the covariate-relevant population characteristics of the human research participants.

Subcutaneous adipose tissue samples were collected from healthy, lean (BMI 26.6 \pm 0.9 kg/m²) kidney donors aged 39 \pm 3.3 years for isolation of primary human adipose-derived mesenchymal stem cells (AdMSCs). AdMSCs were utilized for generation of control and senescent cell conditioned media.

Flow Cytometry Reporting Summary

Form fields will expand as needed. Please do not leave fields blank.

► Data presentation

For all flow cytometry data, confirm that:

- ☒ 1. The axis labels state the marker and fluorochrome used (e.g. CD4-FITC)
- ☒ 2. The axis scales are clearly visible
- ☒ 3. All plots are contour plots with outliers or pseudocolor plots
- ☒ 4. A numerical value for number of cells or percentage (with statistics) is provided

► Methodological details

5. Describe the sample preparation.

1x10⁶ cells were stained with APC-conjugated anti-Cd115 (eBioscience, AFS98, 0.25ug) and PE-conjugated anti-RANK (ThermoFisher Scientific, 9A725, 2ug) in 100uL volume for 30 minutes at 4oC, rotating. Cells were washed in FACS buffer, centrifuged, and resuspended in 500uL 1% paraformaldehyde.

6. Identify the instrument used for data collection.

FACSCalibur, BD Biosciences

7. Describe the software used to collect and analyze the flow cytometry data.

Data was collected with Cell Quest software. Data was analyzed using FlowJo (FlowJo, LLC).

8. Describe the abundance of the relevant cell populations within post-sort fractions.

Not applicable. Flow cytometry was used for analysis only.

9. Describe the gating strategy used.

Unstained and single stained controls were utilized to set gates for Cd115-APC positive vs negative and RANK-PE positive vs negative cell populations.

Tick this box to confirm that a figure exemplifying the gating strategy is provided in the Supplementary Information. ☒